Dual layer electrode liquid crystal lens for 2D/3D tunable endoscopy imaging system

Amir Hassanfiroozi,[1] Yi-Pai Huang,[1,*] Bahram Javidi,[2] and Han-Ping D.Shieh[1]

[1]*Department of Photonics and the Institute of Electro-Optical Engineering/Display Institute, National Chiao Tung University, 30010 Hsinchu, Taiwan*
[2]*Electrical and Computer Engineering Department, University of Connecticut, Storrs, Connecticut 06269-4157, USA*
[*]boundshuang@mail.nctu.edu.tw

Abstract: In this paper, we demonstrate a multi-functional liquid-crystal lens (MFLC-lens) based on dual-layer electrode design. Compared with the previous 3D endoscopes, which use double fixed lens capturing, the proposed LC lens is not only switchable between 2D and 3D modes, but also is able to adjust focus in both modes. The diameter of the MFLC-lens is only 1.42mm, which is much smaller than the available 3D endoscopes with double fixed lenses. To achieve the MFLC-lens, a high-resistance layer needs to be coated on the electrode to generate an ideal gradient electric-field distribution, which can induce a lens-like form of LC molecules. The parameters of high-resistive layer are investigated and discussed with an aim to optimize the performance of the MFLC-lens.

©2016 Optical Society of America

References and links

1. S. Sato, "Liquid-crystal lens-cells with variable focal length," Jpn. J. Appl. Phys. **18**(9), 1679–1684 (1979).
2. M. Ye and S. Sato, "Optical properties of liquid crystal lens of any size," Jpn. J. Appl. Phys. **41**(5B), L571–L573 (2002).
3. S. Sato, "Applications of liquid crystals to variable-focusing lenses," Opt. Rev. **6**(6), 471–485 (1999).
4. T. Nose, S. Masuda, and S. Sato, "A liquid crystal microlens with hole-patterned electrodes on both substrates," Jpn. J. Appl. Phys. **31**(5B), 1643–1646 (1992).
5. M. Ye, B. Wang, and S. Sato, "Liquid-crystal lens with a focal length that is variable in a wide range," Appl. Opt. **43**(35), 6407–6412 (2004).
6. H. Ren, S. T. Wu, "Adaptive liquid crystal lens with large focal length tunability," Opt. Express **14**(23), 11292–11298 (2006).
7. S. Sato, "Liquid-crystal lens-cells with variable focal length," Jpn. J. Appl. Phys. **18**(9), 1679–1684 (1979).
8. B. Wang, M. Ye, M. Honma, T. Nose, and S. Sato, "Liquid crystal lens with spherical electrode," Jpn. J. Appl. Phys. **41**(11A), L1232–L1233 (2002).
9. H. Ren, D. W. Fox, B. Wu, and S.-T. Wu, "Liquid crystal lens with large focal length tunability and low operating voltage," Opt. Express **15**(18), 11328–11335 (2007).
10. M. Ye, S. Hayasaka, and S. Sato, "Liquid crystal lens array with hexagonal-hole-patterned electrodes," Jpn. J. Appl. Phys. **43**(9A), 6108–6111 (2004).
11. H. C. Lin and Y. H. Lin, "A fast response and large electrically tunable-focusing imaging system based on switching of two modes of a liquid crystal lens," Appl. Phys. Lett. **97**(6), 063505 (2010).
12. Y. H. Lin, H. S. Chen, H. C. Lin, Y. S. Tsou, H. K. Hsu, and W. Y. Li, "Polarizer-free and fast response microlens arrays using polymer-stabilized blue phase liquid crystals," Appl. Phys. Lett. **96**(11), 113505 (2010).
13. H. Ren, S. Xu, and S.-T. Wu, "Polymer-stabilized liquid crystal microlens array with large dynamic range and fast response time," Opt. Lett. **38**(16), 3144–3147 (2013).
14. O. Pishnyak, S. Sato, and O. D. Lavrentovich, "Electrically tunable lens based on a dual-frequency nematic liquid crystal," Appl. Opt. **45**(19), 4576–4582 (2006).
15. Y. Y. Kao and P. C. P. Chao, "A new dual-frequency liquid crystal lens with ring-and-pie electrodes and a driving scheme to prevent disclination lines and improve recovery time," Sensors (Basel) **11**(12), 5402–5415 (2011).
16. C.-T. Lee, Y. Li, H.-Y. Lin, and S.-T. Wu, "Design of polarization-insensitive multi-electrode GRIN lens with a blue-phase liquid crystal," Opt. Express **19**(18), 17402–17407 (2011).
17. C. J. Hsu, P. C. P. Chao, and Y. Y. Kao, "A Thin Multi-Ring Negative Liquid Crystal Lens Enabled by High-k Dielectric Material," Microsyst. Technol. **17**(5–7), 923–929 (2011).
18. Y. Li, Y. Liu, Q. Li, and S. T. Wu, "Polarization independent blue-phase liquid crystal cylindrical lens with a resistive film," Appl. Opt. **51**(14), 2568–2572 (2012).

19. M. Ye, B. Wang, M. Yamaguchi, and S. Sato, "Reducing driving voltages for liquid crystal lens using weakly conductive thin film," Jpn. J. Appl. Phys. **47**(6), 4597–4599 (2008).
20. M. Ye, B. Wang, and S. Sato, "Realization of liquid crystal lens of large aperture and low driving voltages using thin layer of weakly conductive material," Opt. Express **16**(6), 4302–4308 (2008).
21. M. Ye, B. Wang, M. Uchida, S. Yanase, S. Takahashi, and S. Sato, "Focus tuning by liquid crystal lens in imaging system," Appl. Opt. **51**(31), 7630–7635 (2012).
22. C.-W. Chen, M. Cho, Y.-P. Huang, and B. Javidi, "Three-dimensional imaging with axially distributed sensing using electronically controlled liquid crystal lens," Opt. Lett. **37**(19), 4125–4127 (2012).
23. Y. Liu, H. Ren, S. Xu, Y. Li, and S. T. Wu, "Fast-response liquid-crystal lens for 3D displays," Proc. SPIE **9005**, 900503 (2014), doi:10.1117/12.2044409.
24. Y.-C. Chang, T.-H. Jen, C.-H. Ting, and Y.-P. Huang, "High-resistance liquid-crystal lens array for rotatable 2D/3D autostereoscopic display," Opt. Express **22**(3), 2714–2724 (2014).
25. V. Urruchi, J. F. Algorri, C. Marcos, and J. M. Sánchez-Pena, "Note: Electrical modeling and characterization of voltage gradient in liquid crystal microlenses," Rev. Sci. Instrum. **84**(11), 116105 (2013).
26. G. Shibuya, H. Yoshida, and M. Ozaki, "High-speed driving of liquid crystal lens with weakly conductive thin films and voltage booster," Appl. Opt. **54**(27), 8145–8151 (2015).
27. M. Kawamura, K. Nakamura, and S. Sato, "Liquid-crystal micro-lens array with two-divided and tetragonally hole-patterned electrodes," Opt. Express **21**(22), 26520–26526 (2013).
28. H. S. Chen and Y. H. Lin, "An electrically tunable endoscopic system by adding a liquid crystal lens to enlarge and shift depth-of-field," Opt. Express **21**(15), 18079–18088 (2013).
29. S. Kuiper, "Electrowetting-based liquid lenses for endoscopy," Proc. SPIE **7930**, 793008 (2011).
30. H.-S. Chen and Y.-H. Lin, "An endoscopic system adopting a liquid crystal lens with an electrically tunable depth-of-field," Opt. Express **21**(15), 18079–18088 (2013).
31. S. W. Seo, S. Han, J. H. Seo, Y. M. Kim, M. S. Kang, N. K. Min, W. B. Choi, and M. Y. Sung, "Microelectromechanical-system-based variable-focus liquid lens for capsule endoscopes," Jpn. J. Appl. Phys. **48**(5), 052404 (2009).
32. Y. H. Lin and H. S. Chen, "Electrically tunable-focusing and polarizer-free liquid crystal lenses for ophthalmic applications," Opt. Express **21**(8), 9428–9436 (2013).
33. M. Ye, B. Wang, M. Uchida, S. Yanase, S. Takahashi, and S. Sato, "Focus tuning by liquid crystal lens in imaging system," Appl. Opt. **51**(31), 7630–7635 (2012).
34. Y. P. Huang, C. W. Chen, and Y.-C. Huang, "Superzone Fresnel Liquid Crystal Lens for Temporal Scanning Auto-stereoscopic Display," IEEE J. Display Technol. **8**(11), 650–655 (2012).
35. H. Li, F. Pan, Y. Wu, Y. Zhang, and X. Xie, "Three-dimensional imaging based on electronically adaptive liquid crystal lens," Appl. Opt. **53**(33), 7916–7923 (2014).
36. H. S. Chen, M. S. Chen, Y. H. Lin, "An electrically tunable depth-of-field endoscope using a liquid crystal lens as an active focusing element," Proc. SPIE 8828, Liq. Cryst. **XVII**, 88281C (2013).
37. A. Hassanfiroozi, Y.-P. Huang, B. Javidi, and H.-P. D. Shieh, "Hexagonal liquid crystal lens array for 3D endoscopy," Opt. Express **23**(2), 971–981 (2015).
38. Y.-J. Wang, X. Shen, Y.-H. Lin, and B. Javidi, "Extended depth-of-field 3D endoscopy with synthetic aperture integral imaging using an electrically tunable focal-length liquid-crystal lens," Opt. Lett. **40**(15), 3564–3567 (2015).
39. M. M. Fenske, Q. Liu, R. J. Sclabassi, and M. Sun, "A Design of a Liquid Crystal Based Single-Lens Stereo Endoscope," in Proceedings of the IEEE 32nd Annual Northeast Bioengineering Conference, April 2006, pp.43–44.
40. P. de Gennes and J. Prost, *The Physics of Liquid Crystal* (Clarendon, 1993).
41. H. De Smet, J. Van den Steen, and D. Cuypers, "Electrical model of a liquid crystal pixel with dynamic, voltage history-dependent capacitance value," Liq. Cryst. **31**(5), 705–711 (2004).
42. J. H. Kim, T.-Y. Seong, S.-I. Na, K.-B. Chung, H.-M. Lee, and H.-K. Kim, "Highly transparent Nb-doped indium oxide electrodes for organic solar cells," J. Vac. Sci. Technol. A **32**(2), 021202 (2014), doi:10.1116/1.4832238.
43. X. Nie, R. Lu, H. Xianyu, T. X. Wu, and S.-T. Wu, "Anchoring energy and cell gap effects on liquid crystal response time," J. Appl. Phys. **101**(10), 103110 (2007), doi:10.1063/1.2734870.
44. S.-J. Hwang, T.-A. Chen, K.-R. Lin, and S.-C. Jeng, "Ultraviolet light treated polyimide alignment layers for polarization-independent liquid crystal Fresnel lenses," Appl. Phys. B **107**(1), 151–155 (2012).
45. S. Dhara and N. V. Madhusudana, "Ionic contribution to the dielectric properties of a nematic liquid crystal in thin cells," N. V. J. Appl. Phys. **90**(7), 3483–3488 (2001), doi:10.1063/1.1388163.
46. A. L. Alexe-Ionescu, G. Barbero, and I. Lelidis, "Complex Dielectric Constant of a Nematic Liquid Crystal Containing Two Types of Ions: Limit of Validity of the Superposition Principle," J. Phys. Chem. B **113**(44), 14747–14753 (2009), doi:10.1021/jp906479w.

1. Introduction

1.1 Tunable liquid crystal lens

Liquid crystal (LC) lenses are active optical elements with electrically tunable focal lengths without any mechanical movements. Because of the large optical anisotropy of this material, the LC director's orientation can be easily controlled by applying low voltage to a nematic

liquid crystal. When an incident plane wave passes through a lens-like phase difference of LC directors, the wave will be converged or diverged depending on the type of voltage applied to the electrodes. The early reports on LC lenses [1–3] used a ratio of the diameter to the cell thickness of about 2~3 for an LC lens optimized to work like a lens.

Extensive research has been conducted on various types of LC lenses. The hole-patterned electrodes [4–7] which have a simple structure with a high optical quality were initially reported. The spherical electrode [8,9] was then proposed to reduce the phase loss which leads to a short focal length. It was followed by hexagonal patterned LC lens [10] in order to have less inactive area and faster response time. To increase the switching time of tunable focusing imaging system [11–13], dual frequency lenses [14,15] were proposed to speed up both the rise and decay times of an LC device.

To further improve the optical performance of LC lens, high-dielectric layer [16,17] was used to smooth the phase profile across the lens without attenuating much electrical potential. However, high-dielectric layer increases the operating voltage to higher than 30volts. Therefore, high-resistive layer [18–27] was applied to generate linearly varying electrical potential from the center to the edge. The high-resistive layer for LC lens successfully demonstrated low operating voltage, fast response time, and high optical performance.

However, the LC-lenses reviewed above were used for 2D imaging tunable systems, which were utilized for 2D endoscope applications in the prior publications [28–31]. In this paper, we propose a new LC-lens structure for both 2D/3D tunable endoscopic applications.

1.2 Endoscopy imaging system

An endoscope is an important tool for medical diagnosis. In general, three main kinds of endoscopic imaging systems are available: rigid endoscopes, flexible endoscopes and capsule endoscopes. Conventional endoscopic systems consisting of several solid lenses suffer from a fixed lens. For practical applications using conventional endoscopes, the doctor may have to move the endoscope back and forth during the examination in order to see a clear image, which may make the patient uncomfortable. The liquid crystal lens is an essential optical device with tunable focal length to replace bulky and solid lenses with voice coil motor. LC-lens also has been used for three-dimensional (3D) endoscope systems [31–39]. 3D vision offers the advantage of improved depth perception and accuracy in the performance of endoscopic surgery, particularly for complex surgical tasks such as suturing.

A key limitation of previous studies is that they do not address the focus tunability of LC lenses when switched into 2D or 3D mode. For example, in early cases of using LC lenses for 3D endoscopy [37], when the LC lens was turned off, the LC lens would act just like a piece of glass. The physician had to move the endoscope back and forth to see a clear image because the LC lens was only able to adjust the focal length in 3D mode and not in 2D mode. Additionally, the prior LC lenses used for endoscopy procedures were using single-layer electrode design, which only have the ability to modulate the focal length in a single mode.

In this paper, the proposed multi-functional LC lens (MFLC-lens), is able to switch to and from 2D and 3D modes, and can further change the focus in both modes. The system is investigated by using dual-layer electrodes and a high resistive transparent film. Table 1 shows a brief comparison between conventional 3D endoscopes (with two fixed solid lenses), LC lenses for 3D endoscopes based on hexagonal arrangement [37], and the proposed endoscopy imaging system using an MFLC lens. The high resistance film is used to minimize the electric field interference of the two electrode layers. To the best of our knowledge, this is the first report describing a "single" LC lens, which can modulate the focal length in both 2D and 3D modes. The proposed LC lens will be mainly used for endoscopic imaging systems.

Table 1. Comparison of the Different Endoscopes

	Conventional endoscope	Hexagonal endoscope	MFLC-lens
Operation based on	2 Solid lenses	7 LC Micro-lenses	1 LC lens & 3 LC Micro-lenses
2D/3D Switchable function	Yes (using 3D glasses)	Yes (computer generated 3D image)	Yes (computer generated 3D image)
2D/3D focus-tunable	No	No	Yes
Distal end outer diameter	10 mm	3.5 mm	2.5 mm
Sketch after the assembly			

2. Basic principle

2.1 Liquid crystal lens

To understand the mechanism of liquid crystal lenses, it is necessary to detail the properties of nematic liquid crystals. The nematic phase is one of the most important phases to produce a liquid crystal lens with a gradient refractive index. Birefringence ascribes to the splitting of a light ray into two components (the ordinary ray and the extraordinary ray) when it enters birefringent materials. These two components have orthogonal polarizations. The refractive index of the ordinary ray is independent of the orientation of the incident ray entering the material. In contrast, the refractive index of the extraordinary ray is dependent on the angle between the incident ray and the orientation of the optical axis of the materials, which depends on the liquid crystal director orientation. Therefore, when the liquid crystal director is tilted, supposing the orientation of the incident ray is fixed, a variation in the refractive index of the extraordinary ray is induced. In liquid crystals, the tilting is attained by use of an electric field. The refractive index presented by the liquid crystals varies between the ordinary index (n_o) and the extraordinary index (n_e) due to the alternations of the director orientation in each area. A mechanical torque is induced due to the elasticity of the nematic liquid. A torque, applied on a particle, influences director deformations in the liquid crystal. Nonzero deformations will result in a nontrivial torque in the director field. The free energy can be minimized using this torque balance, which can be explained by Euler-Lagrange equations. The Poisson equation (or Laplace in regions where the charge density is zero) describes electrostatic potential, which dictates the definition of the electric charge and its density corresponding to the applied electric field. The elastic charges interact via the Coulomb potential which results in a collective macroscopic director reorientation [40]. There is a convergence solution after this interaction, leading us to use the Berreman4x4 matrix method to determine director configuration induced by the interaction. Due to the complexity of this method, Smet's macro-model for LC cells is preferable. The nematic liquid crystal is a long-range orientational order of rod like polar molecules. In a nematic liquid crystal with positive anisotropy under an applied electric field, directors reorient toward electric field direction. In addition, electric field induces a dipole moment density with two components one in direction of extraordinary axis and another along ordinary axis. The balance of the dielectric, viscous, and elastic torques determines the director dynamics, which can affect the response time and operating voltage. Three types of torques which affects liquid crystal molecules are: Elastic ($T_1 = Kx$), Electrical ($T_2 = CE^2$), and Viscosity ($T_3 = \gamma dx / dt$), where K, γ and C are constants. T_1 and T_3 try to tilt the molecule in the opposite direction as T_2. The equilibrium of torques can be written in a well-known first-order system form [41] in which equilibrium equations in a steady state and effective voltage can be easily obtained.
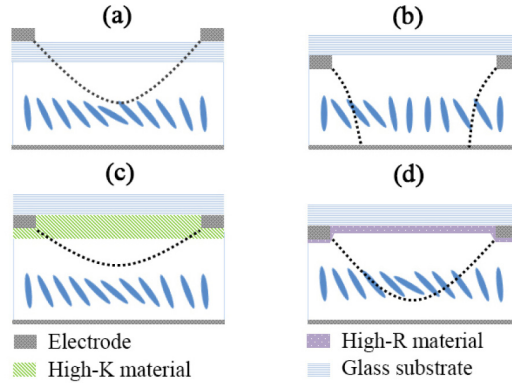
Fig. 1. Cross-section of different LC lens, (a) external electrode LC lens, (b) internal electrode LC lens, (c) LC lens using a high-K layer, (d) LC lens using a high-R layer. The dashed line shows the potential.

2.2 High-resistive material

The orientation of LC directors is determined by potential differences across the two conductive layers at the top and bottom of the liquid crystal. This can change LC lens properties. To make a lens-like effect in a liquid crystal cell a hole-patterned electrode on the glass is designed as shown in Fig. 1(a). However, high driving voltages are required to make a gradient potential from the edge of the LC lens to the center of the LC lens, due to the shielding of the voltage in the glass substrate. If the electrode's position is upside-down as in Fig. 1(b), the required driving voltage is lower, but there is no lens-like distribution of the refractive index. The applied voltages can be lowered using a high dielectric (high-k) layer coated on the hole-patterned electrode to smooth the phase profile across the lens, though a lower applied voltage is still desired. Because of the thickness of this layer (~few μm), high-K layer shields a portion of the applied voltage as in Fig. 1(c). This problem can be solved by using a thin film layer with high-resistivity (high-R) as in Fig. 1(d), which also provides more options to fabricate an LC lens according to aperture size. By adjusting to a proper frequency, the aperture becomes larger the driving frequency becomes lower. When the aperture is small, a higher driving frequency is needed. Thus, making LC lenses with various sizes will be possible with a very low driving voltage.
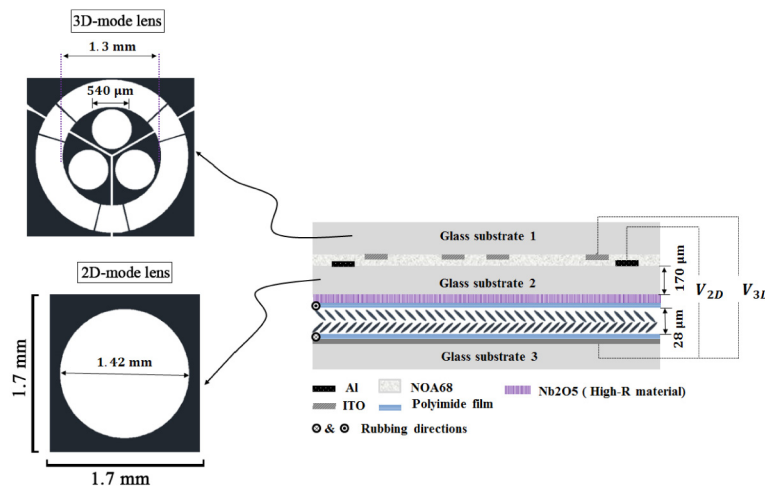

Fig. 2. Top view of the electrode patterns and cross section of the MFLC-LC lens cell.

3. Fabrication

The designed Multi-functional liquid crystal (MFLC) lens is shown in Fig. 2. Two 550 μm glass substrates (glass substrates 1and 3) are coated with 70 nm ITO, then 20 nm SiO2 and a 170 μm glass (glass substrate 2) which is coated with 200 nm Al. One of ITO substrates (glass substrate 1) is etched with the desired three-hole pattern. A thin layer of high-resistive film (niobium pentoxide-Nb2O5) is deposited on the glass substrate 2 (~31 nm) using a radio frequency (RF) magnetron sputtering system. At an RF power of 30W the Nb2O5 film shows the lowest sheet resistance as reported in [42]. With this result, we set the RF power to 30W, as the voltage would drop close to the electrode if the impedance was too high.

The UV curable resin (NOA68) fills in the space (15μm) between the glass substrate 1 and the glass substrate 2. The polyimide (PI) layer is coated on the glass substrates 2 and 3 as an alignment layer. A UV ozone surface treatment is used to clean and modify the molecular surface of the alignment layer. Anchoring phenomena are responsible for restoring the director orientation in an LC lens when the electric field is switched off. When the electric field is switched on, anchoring prevents the LC molecules from being completely reoriented. The anchoring energy plays an important role in affecting the LC response time. Within the weak anchoring regime, the LC decay time is inversely proportional to the anchoring energy. If we can find a polyimide that has somewhat larger anchoring with the LC material, then the decay time can be improved [43]. The polar anchoring energy of LC molecules on UV-treated PI alignment layers is reported in [44] to have a faster LC lens; the substrates undergo UV-treatment (at 21.7 mW/cm^2) for 20 minutes. Finally, these two PI layers are rubbed anti-parallel in order to form the micro-grooved alignment surface, resulting in a pretilt angle of about 2°. The two glasses are then stacked with a 28um microsphere spacer between them. The cell was filled with E7 at a temperature higher than the isotropic-nematic phase transition to avoid the appearance of gas bubbles and disclination lines to enhance the alignment of the layers. The parameters of the nematic E7 are: $k_{11}/k_{33} = 1.54$, $k_{22}/k_{11} = 0.93$ for $\lambda_0 = 435nm$, $n_e = 1.8208$ and $n_o = 1.544$. The quality of alignment layer with different applied voltages is shown in Fig. 3. The alignment layers function the same as different voltages applied to the cell, which yields a good stability of these layers.

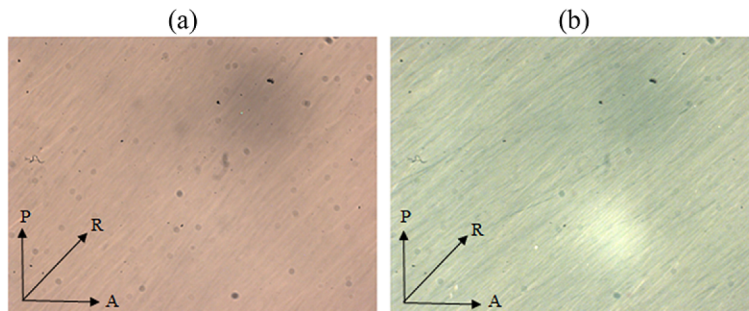(a)   (b)

Fig. 3. POM image of rubbing quality at different voltages (a) 4 Vrms (b) 8 Vrms; P: the transmission axis of the polarizer, A: the transmission axis of the analyzer, R: the direction of alignment of the substrate.

4. Experimental results and discussion

Liquid crystals are dielectric materials; however, due to ionic impurities, they usually have nonzero value of conductivity σ. E7 has a typical conductivity of $\sim 10^{-11} \Omega - m$. The dielectric constant is given as a complex quantity, $\varepsilon^* = \varepsilon' - j\varepsilon''$ where ε' is the real part of the dielectric constant and ε'' is the dielectric loss factor of the medium with $j = \sqrt{-1}$. The dielectric dispersion spectrum of a nematic liquid crystal depends on the direction of the

applied field with respect to the director ($\hat{n}$). When $\vec{E} \parallel \hat{n}$, the relaxation frequency decreases to fairly low values (in the range of few kHz to a few MHz). For $\vec{E} \perp \hat{n}$, the relaxation frequency is in the GHz range. At very low frequencies (≤1kHz), the ionic impurity also contributes to the dielectric properties. The effect of ion impurities grows very large, that is, $\omega^{-3/2}$ for the real part and ω^{-1} for the imaginary part [45]. The complex dielectric constant of the LC cell can be written as following formulas [46]:

$$\varepsilon' = \frac{\varepsilon_{eq}}{1 + \omega^2 \left(\dfrac{\varepsilon_{eq}}{\sigma_{eq}} \right)^2} \tag{1}$$

$$\varepsilon'' = \frac{\omega(\varepsilon_{eq}/\sigma_{eq})}{1 + \omega^2 \left(\dfrac{\varepsilon_{eq}}{\sigma_{eq}} \right)^2} \varepsilon_{eq} \tag{2}$$

where σ_{eq} and ε_{eq} are equivalent conductivity and equivalent dielectric constant, respectively. When the LC lens is switched on, the potential distribution of high resistive thin film can be obtained as a differential equation [18]:

$$\nabla^2 V = \frac{\rho_R}{d_R} \left(\frac{\omega\varepsilon'}{d_{LC}} jV + \frac{\omega\varepsilon''}{d_{LC}} V \right) \tag{3}$$

In Eq. (3), ρ_R is the resistivity of the resistive film, d_R and d_{LC} are the thicknesses of the resistive film and LC, respectively, ω is the AC frequency, and ε' and ε'' are the real and imaginary parts of LC dielectric constants. A general solution for the Eq. (3) is obtained by substituting Eq. (1) and Eq. (2) into Eq. (3), respectively. When solving the differential equation, analytic solution can be difficult. We found the optimized parameters of the high-R layer such as the ratio of resistivity of high-R layer to its thickness ($0.03 < \rho_R (\Omega - m)/d_R (nm) < 0.3$) with proper frequency range (10 kHz<f<70 kHz).

4.1 Optimizingh high-R layer parameters

As discussed above, Eq. (3) becomes a complicated equation to solve analytically after substituting Eq. (1) and Eq. (2) into Eq. (3), especially when looking for proper thickness, resistivity and frequency. Therefore, we prepared ten samples varied by resistivity and thickness to find a proper frequency to operate the LC lens as shown in Table 2. The sheet resistance of the samples was measured by Mitsubishi Hiresta-UP MCP HT450 using a URS standard probe. The Atomic Force Microscope (AFM) images of the deposited Nb2O5 with different conditions [see Table 2] are shown in Fig. 4 to indicate the surface roughness of samples. From the measurement results, all the surfaces are smooth and uniform with root mean square (RMS) roughnesses in the sub-nm range (0.3nm to 0.5nm), and the numbers are shown in Table 2.

We prepared a single hole liquid crystal (LC) lens with a diameter of about 2 mm. To investigate the LC lens performance, interference patterns were measured using two cross polarizers when LC lenses were placed between them. Figure 5 demonstrates the LC lens fringe patterns when they are applied with 1 kHz driving frequency and 6 Vrms. Figure 5 clearly presents that most of the samples show interference patterns only on the edge of lens, which cannot form an ideal lens profile. Furthermore, Sample 4 and Sample 7 did not respond to the applied voltage (6Vrms) when the function generator was set to a 1 kHz output frequency. But when we increased the frequency from 1 kHz to 66 kHz, we found that only

Sample 4 and 7 can generate an ideal lens profile, as shown in Fig. 6. It should be noted that there was no lens effect for other samples even at higher frequencies (1 kHz – 66 kHz).

Table 2. Condition of Sputtering Nb2O5 and Key Parameters of Nb2O5 for 10 Samples and AFM Data. RMS: Root Mean Square of Roughness.

| Sample	O2 gas	Annealing (350°)	AFM (RMS)	Thickness(d)	$\rho(\Omega\text{-m})$	ρ/d (Ω-m/nm)	Working frequency
1	None	None	0.362 nm	12 nm	1.26×10^5	10500	N/A
2	None	Yes	0.384 nm	12 nm	2.31×10^5	19300	N/A
3	1 sccm	Yes	0.328 nm	6 nm	5.08×10^2	84.800	N/A
4	None	None	0.487 nm	31 nm	1.00×10^1	0.324	10-15 kHz
5	None	Yes	0.511 nm	31 nm	4.18×10^5	13500	N/A
6	3 sccm	Yes	0.415 nm	3 nm	1.05×10^2	35.100	N/A
7	None	None	0.443 nm	50 nm	1.94×10^0	0.038	33-66 kHz
8	None	Yes	0.452 nm	50 nm	1.36×10^5	2730	N/A
9	3 sccm	Yes	0.249 nm	5 nm	2.83×10^1	5.6700	N/A
10	Without Nb2O5						
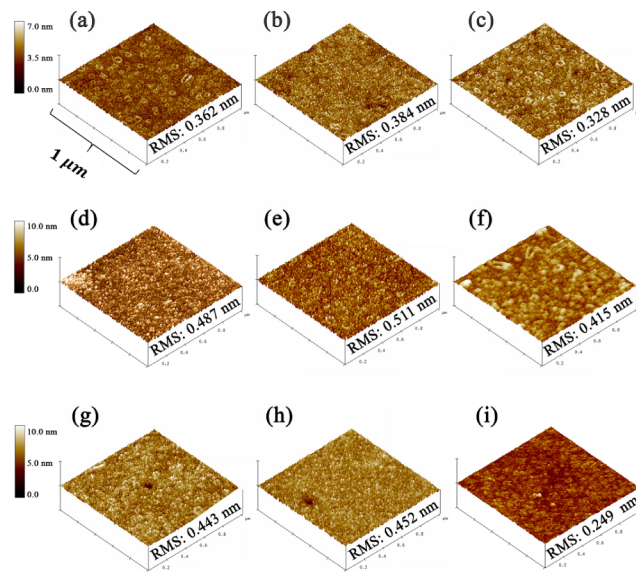
Fig. 4. AFM image of the Nb2O5 roughness for (a) sample 1, (b) sample 2, (c) sample 3, (d) sample 4, (e) sample 5, (f) sample 6, (g) sample 7, (h) sample 8 and (i) sample 9, [See Table 2], scan size is 1μm × 1μm.

Obviously, when a highly- resistive layer (in this case Nb2O5) is used for LC-lens, the ratio of ρ/d has to be well controlled. In the experiment, the ρ/d of sample 4 and 7 are 0.324 and 0.038, respectively. From the results, the samples will be workable when the frequency range is 10 - 15 kHz and 33- 66 kHz, as shown in Fig. 6. Thus, after we determine the frequency according to the device compatibility we can change the applied voltage to change the focal length of the LC lens. Finally, Sample 4 was chosen, because it could work at lower frequency, and can results in lower power consumption. Moreover, most devices are

adapted to human audible frequency (20 Hz - 20 kHz); therefore, electronics are made to produce a frequency lower than 20 kHz.
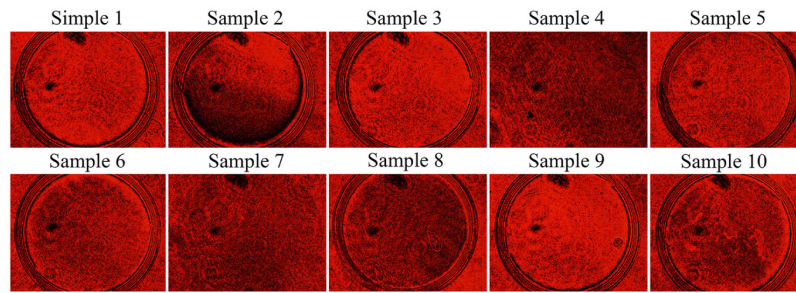

Fig. 5. Interference patterns for LC lens at driving frequency of 1 kHz for Sample 1-10. The applied voltage is 6.0 Vrms.
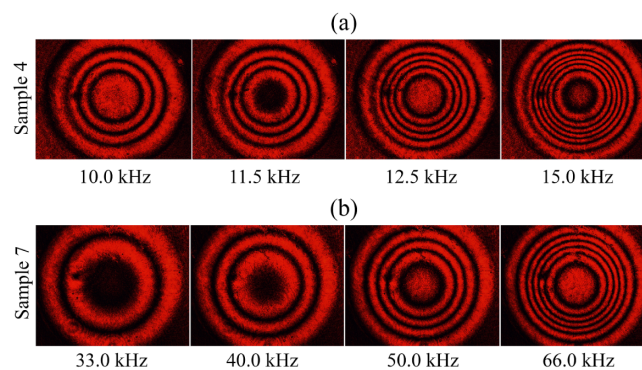

Fig. 6. Interference patterns at driving frequencies of 10 kHz, 11.5 kHz, 12.5 kHz and 15 kHz for sample 4 (a) and driving frequency of 33 kHz, 40 kHz, 50 kHz and 66 kHz for sample 7 (b). The applied voltage is 6.0 Vrms.

In Fig. 6, we conclude that a suitable driving frequency with a ratio of ρ/d is required to operate an LC lens at low applied voltage. In the study above on Nb2O5 we found that all these parameters are applicable to lowering the driving voltage and improving performance of multi-functional liquid crystal (MFLC) lenses. All the parameters were optimized in sample 4, therefore, we utilize these parameters such as ρ/d ratio and its working frequencies for MFLC lens as explained in the following section.

4.2 Optical performance of the MFLC-lens

In this section, the properties of MFLC lenses are investigated using an interference method. The MFLC cell is placed between two crossed polarizers in which the rubbing direction makes an angle of 45° with respect to each polarizer. A beam from a helium-neon (He-Ne) laser operating at 632 nm is expanded and passes through the MFLC-lens placed between two crossed polarizers, as shown in Fig. 7(a). The liquid crystal is birefringent, which means that different polarizations of light travel at different speeds through it, and are refracted differently. The first polarizer contains both types of ordinary and extraordinary waves. When the waves pass through the liquid crystal, the ordinary wave experiences a spatial phase shift but the extraordinary wave experiences a spatially varying phase shift. When these two waves exit the liquid crystal, their phases are different. Finally, when they pass through the second polarizer, interference will occur. The retardation difference of the two adjacent constructive or destructive interference rings indicates a phase change of 2π. Furthermore, the variation in

phase retardation induced by the applied voltage shows how the electrical field alters the lens properties.
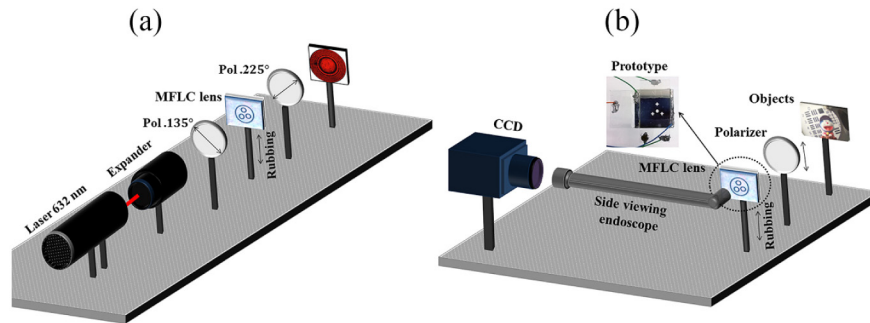

Fig. 7. (a) Experimental setup for measuring the properties of MFLC-lens. (b) Experimental setup for capturing images using a side viewing endoscope. Pol: Polarizer.

Figure 8(a) shows the interference patterns present in the 2D mode when the MFLC-lens is used with $V_{2D} = 0 \sim 12.5 V_{rms}$ (1 kHz). In this mode only the large circular lens is activated as increasing the applied voltage, the number of the circular interference fringes changes and the property of the MFLC lens is electrically controllable. When a 3D image is desired and multiple perspective images are needed, the electrodes in the MFLC-lens will switch to the first layer of electrode from the second layer in which there are three lenslets available. As shown in Fig. 8(b), the 3D lenses are obtained by applying $V_{3D} = 0 \sim 8.5 V_{rms}$ (1 kHz).
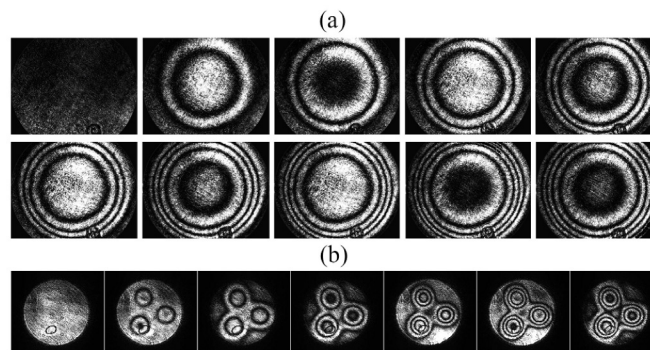

Fig. 8. Interference pattern when MFLC-lens is used with different voltages (a) for 2D mode 0~12.5 Vrms (b) for 3D mode 0~8.5 Vrms.

The fringe patterns are recorded by means of a CCD sensor and the image intensity is enhanced. Figure 9 shows the phase difference distribution of the MFLC-lens in the direction of rubbing calculated for both 2D and 3D modes based on counting the interference fringes at their position from the center to edge of the MFLC lens. In Fig. 10, the voltages applied to the electrodes are the same as the applied voltages in Fig. 8(a) and (b). It should be noted that the estimated phase distribution parallel to the rubbing direction is the same as the phase distribution in other directions. Because of its perfect circular interference rings, no aberrations are expected.

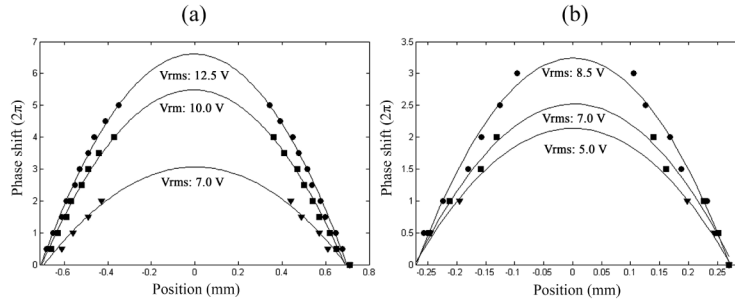(a)   (b)

Fig. 9. Voltage dependence of phase shift for 2D LC lens (a), 3D LC lens (b).

In Fig. 10(a) the focal length of the measured phase profiles are shown as a result of the phase shift from 0 to 10π radians for voltages from to when the 2D mode is activated. The focal length of the MFLC-lens in 3D mode that results from the phase shift from 0 to 6π radians for voltages from to is shown in Fig. 10(b). It is noted that the niobium pentoxide (Nb2O5) has a high dielectric constant (~41) and has having high resistivity. Therefore, we expect this layer to smooth the phase profile even when the MFLC-lens is not applied with a proper frequency, which can make the high-R layer active. Therefore, if we change the driving frequency from 1 kHz to 12 kHz for this cell, we can achieve the same phase profile with 2.5X times lower applied voltage for the same cell gap. A proper frequency can decrease the applied voltage. For the sample in Fig. 1(a), for 2 mm aperture diameter and a glass substrate of 550 μm with cell gap of 28 μm, the voltage is from 55 to 6.0 when the frequency is 16 kHz. The measured response time of the MFLC lens for 2D and 3D mode was 600ms and 740ms, respectively. Switching time from 2D/3D modes is about 1.5 seconds. The response time could be faster if a liquid crystal material with higher birefringence was used.

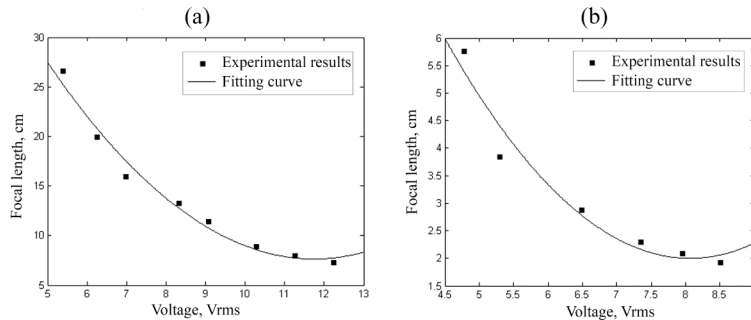(a)   (b)

Fig. 10. Focal length as a function of the applied voltage for 2D LC lens (a), 3D LC lens (b).

Figure 11 shows six images of the ISO 3334 test chart when the position of the chart is located at different distances from the MFLC-lens and when the MFLC-lens is on or off. In Fig. 11(a), the test chart location is 80 mm from the lens with a driving voltage of $12.5 V_{rms}$. In Fig. 11(b), the test chart location is 125 mm from the lens with driving voltage of $8.5 V_{rms}$. In Fig. 11(c), the location is in 180 mm with driving voltage of $6.8 V_{rms}$. The optical power adjustment of the MFLC-lens brings the object into focus, which leads to a sharp and clear image. Figure 7(b) illustrates the experimental setup we used to capture the images using a side viewing endoscope, for captured images shown in Fig. 11(d). Each MFLC-lens can focus on the different depths of an object as the applied voltage varies without any movement for the image sensor or the CCD. The sectional 2D images can be achieved at arbitrary depth positions by altering the focal length of the MFLC-lens. The depth information data was obtained by capturing several 2D images of the 3D object. When the MFLC-lens is switched

to 3D mode, each lens can capture a 2D image of the 3D object from different angles at varying tunable depths. Therefore, the system can record the depth information of the image by properly synchronizing the 2D images. A rudimentary 3D image reconstructed from a set of 2D images after object segmentation, image alignment and depth map generation is shows in Fig. 11(e).
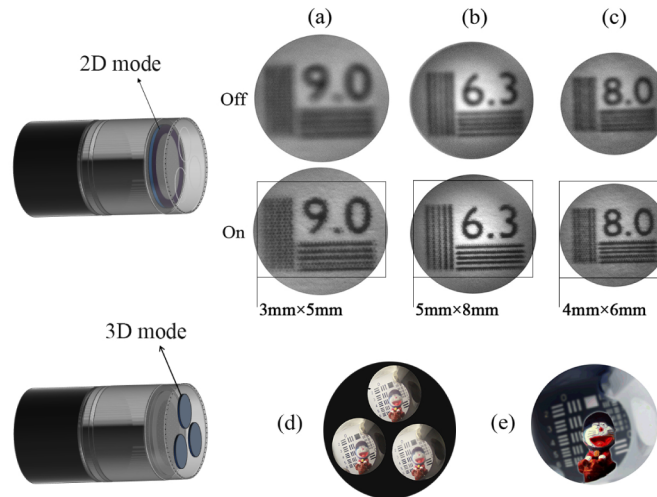

Fig. 11. Image performance of the MFLC-lens for different distance of ISO 3334 test chart from the MFLC-lens when lens is on and off. Distance and voltage values are: (a) 80 mm/ 12.5Vrms (b) 125 mm/ 8.5Vrms (c) 180 mm/ 6.8Vrms. (d) three 2D images taken to construct a 3D image shown in (e).

5. Conclusion

A three-dimensional (3D) imaging system is an important technology for objects in close proximity sensing, such as endoscopy. In this paper, a multi-functional liquid-crystal lens (MFLC-lens) is demonstrated for 2D and 3D switchable function. Importantly, this MFLC-lens can further modulate the focal length without mechanical movement in both 2D and 3D modes. To achieve multiple focal length lens functions, a novel structure with dual-layer electrode coated by a high resistive transparent film was developed. The resistivity and thickness of high-R layer and proper operating frequency were optimized for the MFLC-lens. The diameter of the proposed MFLC-lens is only 1.42mm with tunable focal length from infinity to 80mm. It can be easily applied to micro-imaging systems, and objects in close proximity sensing for both 2D and 3D image capturing. Applications may include medical imaging, endoscopy, robotics, and cell phones.

Acknowledgment